Discovery, TESS Characterization, and Modeling of Pulsations in the Extremely Low-mass White Dwarf GD 278

Isaac D. Lopez[1,2], J. J. Hermes[2], Leila M. Calcaferro[3,4], Keaton J. Bell[5,8], Adam Samuels[2], Zachary P. Vanderbosch[6], Alejandro H. Córsico[3,4], and Alina G. Istrate[7]

[1] High Point University, Department of Physics, One University Parkway, High Point, NC 27268, USA; ilopez1@highpoint.edu
[2] Department of Astronomy & Institute for Astrophysical Research, Boston University, 725 Commonwealth Ave., Boston, MA 02215, USA
[3] Grupo de Evolución Estelar y Pulsaciones, Facultad de Ciencias Astronómicas y Geofísicas, Universidad Nacional de La Plata, Paseo del Bosque s/n, 1900, La Plata, Argentina
[4] Instituto de Astrofísica La Plata, CONICET-UNLP, Paseo del Bosque s/n, 1900, La Plata, Argentina
[5] DIRAC Institute, Department of Astronomy, University of Washington, Seattle, WA 98195, USA
[6] Department of Astronomy, University of Texas at Austin, Austin, TX 78712, USA
[7] Department of Astrophysics/IMAPP, Radboud University, PO Box 9010, 6500, GL Nijmegen, The Netherlands

Abstract

We report the discovery of pulsations in the extremely low-mass (ELM), likely helium-core white dwarf GD 278 via ground- and space-based photometry. GD 278 was observed by the Transiting Exoplanet Survey Satellite (TESS) in Sector 18 at a 2 minute cadence for roughly 24 days. The TESS data reveal at least 19 significant periodicities between 2447 and 6729 s, one of which is the longest pulsation period ever detected in a white dwarf. Previous spectroscopy found that this white dwarf is in a 4.61 hr orbit with an unseen $>0.4\,M_\odot$ companion and has $T_{\rm eff} = 9230 \pm 100$ K and $\log g = 6.627 \pm 0.056$, which corresponds to a mass of $0.191 \pm 0.013\,M_\odot$. Patterns in the TESS pulsation frequencies from rotational splittings appear to reveal a stellar rotation period of roughly 10 hr, making GD 278 the first ELM white dwarf with a measured rotation rate. The patterns inform our mode identification for asteroseismic fits, which, unfortunately, do not reveal a global best-fit solution. Asteroseismology reveals two main solutions roughly consistent with the spectroscopic parameters of this ELM white dwarf, but with vastly different hydrogen-layer masses; future seismic fits could be further improved by using the stellar parallax. GD 278 is now the tenth known pulsating ELM white dwarf; it is only the fifth known to be in a short-period binary, but is the first with extended, space-based photometry.

Unified Astronomy Thesaurus concepts: White dwarf stars (1799); ZZ Ceti stars (1847); Asteroseismology (73); Stellar pulsations (1625)

1. Introduction

White dwarf stars represent the final evolutionary state of main-sequence stars with masses $\lesssim 8$–$10\,M_\odot$, and are the end stages for $\sim$98% of all stars in the Milky Way. The observed mass distribution of spectroscopically confirmed hydrogen-atmosphere (DA) white dwarfs from the Sloan Digital Sky Survey (SDSS) peaks around $0.6\,M_\odot$, with smaller distributions within both tail ends, the smaller of which peaks around $0.4\,M_\odot$ (e.g., Kepler et al. 2007; Tremblay et al. 2011). The lower mass limit for isolated white dwarfs is $\sim$0.4 $M_\odot$ (Kilic et al. 2007), constrained by the age of the Milky Way. Therefore, the progenitors of extremely low-mass (ELM; $\lesssim 0.3\,M_\odot$) white dwarfs must have been giant stars that experienced enhanced mass loss due to a close companion, the first episode of which occurred on the first ascent of the red-giant branch (Marsh et al. 1995; Driebe et al. 1998). This process can occur in a close binary, where the progenitor star transfers mass either via Roche lobe overflow (Iben & Tutukov 1986) or a common-envelope event (Paczynski 1976; Iben & Livio 1993).

DAV stars (also called ZZ Ceti stars) are variable white dwarfs that undergo pulsations in a narrow temperature range where a convection zone forms, from roughly 12,500 K to 10,000 K in canonical-mass ($0.6\,M_\odot$) white dwarfs. These global, non-radial g-mode pulsations are driven by partially ionized regions that form within their atmospheres. These pulsations manifest as optical variations of up to 30% and offer the unique opportunity to probe their interiors via asteroseismology (Winget & Kepler 2008; Fontaine & Brassard 2008; Althaus et al. 2010; Córsico et al. 2019).

Pulsations have previously been observed in nine ELM white dwarfs (Hermes et al. 2012, 2013a, 2013b; Bell et al. 2015, 2017, 2018; Pelisoli et al. 2018b; Guidry et al. 2021), including one with a millisecond pulsar companion (Kilic et al. 2015, 2018). These discoveries effectively extend the DAV instability strip to lower surface gravities and cooler temperatures ($6.0 \lesssim \log g \lesssim 6.8$ and $7800\,{\rm K} \lesssim T_{\rm eff} \lesssim 10,000\,{\rm K}$). This low-mass extension likely also contains contaminants, especially metal-poor A stars (Pelisoli et al. 2018a, 2018b), in contrast to the space occupied purely by classical DAVs at higher masses (e.g., Bell et al. 2017).

Most of the known radial-velocity-confirmed ELM white dwarfs were discovered by the ELM Survey (Brown et al. 2010, 2012, 2013, 2016, 2020; Kilic et al. 2011, 2012; Gianninas et al. 2015), a targeted spectroscopic search for ELM white dwarfs, which has discovered 98 double-white-dwarf binaries within the SDSS footprint. An additional eight ELM white dwarfs were reported by Kosakowski et al. (2020), as part of an extension of the ELM Survey into the southern hemisphere. This southern extension relies on photometry from the VST ATLAS and SkyMapper surveys, and also employs a Gaia astrometry-based selection, which chooses candidates from a unique region of parallax-magnitude space occupied by known ELM white dwarfs.

---

[8] NSF Astronomy and Astrophysics Postdoctoral Fellow.

The population of ELM white dwarfs represent a collection of objects that contribute to a steady foreground of gravitational waves. The sensitivity of the future Laser Interferometer Space Antenna (LISA) observatory is expected to be set by the noise floor from unresolved double-white-dwarf binaries (Amaro-Seoane et al. 2017). Identifying and characterizing compact binary systems in the Milky Way will help characterize the noise floor that may otherwise impede on LISA's ability to detect gravitational waves.

The field of white dwarf astronomy is currently undergoing a transformation thanks to space-based missions such as Gaia (Gaia Collaboration et al. 2016) and the Transiting Exoplanet Survey Satellite (TESS; Ricker et al. 2015). With the release of Gaia DR2, the number of white dwarfs we now know about has exploded from $\sim$33,000 to $\sim$260,000 (Gentile Fusillo et al. 2019), including a large catalog of candidate ELM white dwarfs (Pelisoli & Vos 2019).

TESS has completed its initial 2 yr mission to observe $\sim$85% of the celestial sphere in search of small planets orbiting nearby stars. Observations were split over 26 24×96 deg^2 sectors, each of which was observed for roughly 27 days. TESS delivered full-frame images at a 30 minute cadence, as well as 2 minute cadence data for select objects as part of their Guest Investigator and Director's Discretionary Targets programs. The 2 minute cadence observations give the opportunity for continuous monitoring of bright white dwarfs ($V \lesssim 16.5$ mag), which both provide much-needed follow-up observations and, due to the near 27 day continuous observations, give excellent opportunities to unambiguously determine periods without aliasing and with precision sufficiently high for reliable asteroseismology.

In this paper, we present the discovery of pulsations in the ELM white dwarf GD 278 via high-speed optical photometry. We also present frequency analysis of the TESS observations, including asteroseismic modeling of the frequency solution we obtain. The rest of this paper is organized as follows: Section 2 describes how GD 278 was selected for follow up and describes the observations, Section 3 presents the frequency analysis of the TESS data, asteroseismic modeling of GD 278 is presented in Section 4, and a discussion and conclusions from this discovery are given in Section 5.

2. Observations

GD 278 (WDJ013058.07+532139.71, $G = 14.9$ mag) was selected for follow-up observations from the Gentile Fusillo et al. (2019) Gaia DR2 catalog of white dwarfs based on its location on the Hertzsprung–Russell (HR) diagram relative to other known pulsating ELM white dwarfs and on its intrinsic variability, which we estimated from its empirically determined G-band flux uncertainty (Guidry et al. 2021). Objects that are intrinsically variable (e.g., pulsators, cataclysmic variables, eclipsing binaries) may have anomalously large flux uncertainties at a given magnitude. With this technique, we estimate GD 278 to be among the top 1% most variable white dwarfs within 200 pc, prompting us to obtain high-speed photometry. Shortly after our increased interest in GD 278, it was published as an ELM white dwarf in a 4.61 hr single-lined spectroscopic binary by the ELM Survey (Brown et al. 2020).

2.1. McDonald Observations

Discovery high-speed photometry was obtained with the 2.1 m Otto Struve telescope at McDonald Observatory near Fort Davis, TX. Observations were obtained over three nights in 2019, all using the frame-transfer ProEM instrument and a red-cutoff *BG40* filter to reduce sky noise. Exposure times were 5 s on 2019 August 2 and 15 s on 2019 September 29 and 2019 November 6. Skies were clear with $1''$–$2''$ seeing, with the exception of the 2019 November data, which were affected by poor weather.

Bias, dark, and dome-flat frames were also obtained at the beginning of each night. We reduced the science frames using standard IRAF packages and procedures (Tody 1986). Flux values of the target star were divided by a bright comparison star in order to perform differential photometry. Data from the McDonald observations are shown in Figure 1.

Highly discrepant points due to bad weather have been clipped by hand and the times have been barycentric-corrected using the software routine `barycorrpy` (Kanodia & Wright 2018).

2.2. TESS Observations

Based in part on our detection of variability from McDonald Observatory, we submitted a TESS Director's Discretionary Time (DDT) proposal (PI: Lopez) to secure 2 minute photometry of candidate variable ELM white dwarfs. This included GD 278 (TIC 308292831, $T = 14.8$ mag), which was observed by TESS in Sector 18 (2019 November 2–27) by Camera 2, temporarily overlapping with our data obtained at McDonald Observatory on 2019 November 6. TESS delivered a 11×11 target pixel file for GD 278 at a 2 minute cadence, with the first mid-exposure time (t_0) starting at BJD 2458790.66104. Data were accessed and downloaded using the Python package `lightkurve` (Lightkurve Collaboration et al. 2018). We tested different apertures for light-curve extraction, but found no improvement over the four-pixel aperture determined by the Science Processing Operations Center (SPOC) pipeline, which we adopt for our analysis.

An 8 day sample of the GD 278 TESS photometry is presented in Figure 2. For visual clarity, the data have been smoothed with a 7 point moving average. Crowding is a factor for the large TESS plate scale (the SPOC pipeline estimates that 42% of the flux in the chosen aperture is coming from GD 278), but this amplitude correction from flux dilution has been applied to our final adopted PDCSAP light curve.

3. Analysis

3.1. Frequency Solution of the TESS Observations

GD 278 exhibits an irregular pulsation pattern with up to 25% peak-to-peak brightness variations in both the McDonald and the TESS light curves. In order to determine the frequency components contributing to the observed light curve, we employed the Python package `Pyriod`,[9] a period detection and fitting software that utilizes a Lomb–Scargle periodogram (Bell 2020). In Table 1, we list 19 frequencies ($f_a, f_b, ..., f_s$) that we detect with significance in the TESS data, which we interpret as independent pulsation modes occurring within the white dwarf GD 278. Properties of these modes that we include
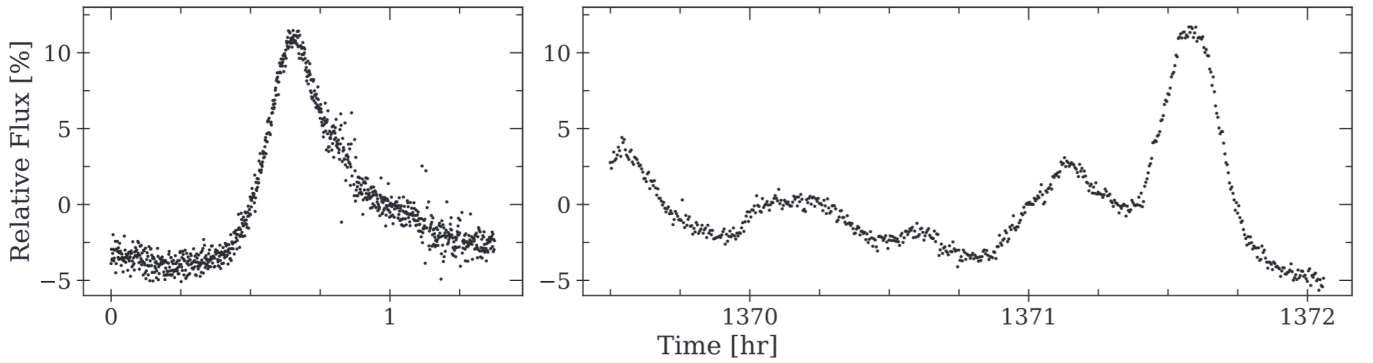
---

[9] http://www.github.com/keatonb/Pyriod

Figure 1. High-speed photometry taken with the 2.1 m Otto Struve telescope at McDonald Observatory, identifying pulsations on 2019 August 2 (left) and confirming them on 2019 September 29 (right) in the extremely low-mass white dwarf GD 278.
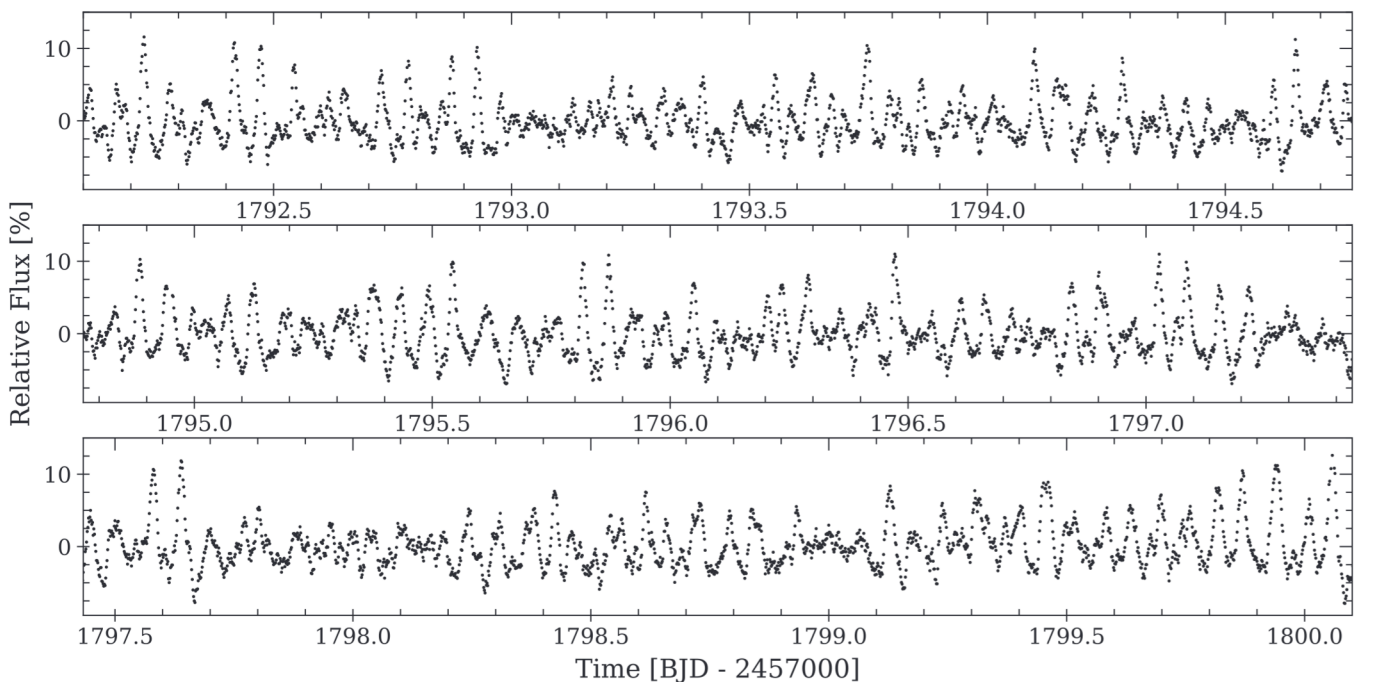

Figure 2. An 8 day sample TESS photometry of the new pulsating extremely low-mass white dwarf GD 278, which was observed in Sector 18. The 2 minute cadence data have been smoothed with a 7 point moving average.

in Table 1 are their periods, frequencies, amplitudes, phases (relative to the t_0 in Section 2.2) and associated uncertainties. The dominant frequency f_a is located at 190.36 μHz and has an amplitude 6.32 times the significance threshold (described below). We find one combination frequency within this set, occurring at the location f_a+f_c, which is likely not a natural oscillation but rather a nonlinear artifact (e.g., Wu 2001).

The periodogram of the TESS data is shown in black in Figure 3, which was used as input to determine the periods in Table 1. In gray we show a periodogram of the TESS data after prewhitening by the list of adopted frequencies in Table 1. The red dashed line represents the 0.1% false alarm probability threshold; peaks above this value have a low probability (<0.1%) of resulting from random noise and are likely intrinsic to the star. We bootstrapped the value of this threshold by keeping the time sampling the same but each time randomly selecting fluxes from the set of flux values. After 10^4 iterations, the false alarm probability threshold was taken to be the value of

the tenth highest amplitude within the ensemble of periodograms and has a value of 0.34%.

In some cases, we chose not to consider certain peaks due to their proximity to other peaks with very high amplitudes that we took to be independent modes. For example, we do not consider the two peaks located at 186.4 μHz and 188.1 μHz, due to their proximity to the peak located at 190.36 μHz. This mode is one of the lowest-frequency pulsations in GD 278, which may lose phase coherence in the same way that lower-frequency modes do in normal-mass DA white dwarfs (Hermes et al. 2017; Montgomery et al. 2020). Thus, these residual peaks to slightly lower frequencies from f_{6c} may not be independent modes themselves, but rather artifacts from the phase incoherence and amplitude variations of the high-amplitude pulsation.

3.2. Simultaneous McDonald and TESS Observations

The 2019 November data from McDonald Observatory were obtained simultaneously while GD 278 was being observed by

Table 1
The 19 Significant Pulsation Periods/Frequencies, One Nonlinear Combination Frequency ($f_a + f_c$), and the Orbital Frequency (f_{orb}) Detected within the GD 278 TESS Data, along with Their Measured Amplitudes, Phases (Relative to BJD 2458790.66104), and Associated Errors

ID	Period (s)	Frequency (μHz)	Amplitude (%)	Phase
f_a	5253.23 ± 0.19	190.359 ± 0.007	2.15 ± 0.06	0.503 ± 0.004
f_b	3365.56 ± 0.14	297.127 ± 0.012	1.25 ± 0.06	0.836 ± 0.007
f_c	4028.83 ± 0.21	248.211 ± 0.013	1.19 ± 0.06	0.508 ± 0.007
f_d	5814.8 ± 0.7	171.975 ± 0.021	0.71 ± 0.06	0.528 ± 0.013
f_e	4628.8 ± 0.5	216.039 ± 0.022	0.67 ± 0.06	0.798 ± 0.013
f_f	5550.6 ± 0.8	180.161 ± 0.025	0.61 ± 0.06	0.681 ± 0.015
f_g	6295.4 ± 1.0	158.846 ± 0.026	0.58 ± 0.06	0.206 ± 0.015
f_h	4428.5 ± 0.5	225.812 ± 0.028	0.53 ± 0.06	0.012 ± 0.017
f_i	5198.3 ± 0.8	192.370 ± 0.029	0.53 ± 0.06	0.986 ± 0.017
f_j	4259.1 ± 0.5	234.79 ± 0.03	0.50 ± 0.06	0.470 ± 0.018
f_k	5896.9 ± 1.0	169.58 ± 0.03	0.48 ± 0.06	0.982 ± 0.018
f_l	5135.1 ± 0.8	194.74 ± 0.03	0.47 ± 0.06	0.063 ± 0.019
f_m	4756.5 ± 0.7	210.24 ± 0.03	0.47 ± 0.06	0.440 ± 0.019
f_n	2447.86 ± 0.18	408.52 ± 0.03	0.46 ± 0.06	0.086 ± 0.019
f_o	6729.0 ± 1.8	148.61 ± 0.04	0.38 ± 0.06	0.865 ± 0.024
f_p	4959.6 ± 1.0	201.63 ± 0.04	0.37 ± 0.06	0.483 ± 0.024
f_q	4093.8 ± 0.7	244.27 ± 0.04	0.37 ± 0.06	0.115 ± 0.024
f_r	2658.51 ± 0.28	376.15 ± 0.04	0.35 ± 0.06	0.028 ± 0.026
f_s	3591.3 ± 0.5	278.45 ± 0.05	0.34 ± 0.06	0.664 ± 0.026
f_a+f_c	2280.15 ± 0.15	438.567 ± 0.028	0.54 ± 0.06	0.816 ± 0.017
f_{orb}	16611 ± 8	60.20 ± 0.03	0.46 ± 0.06	0.091 ± 0.019

Note. Each detection has an amplitude above the 0.1% false alarm probability threshold of 0.34%.
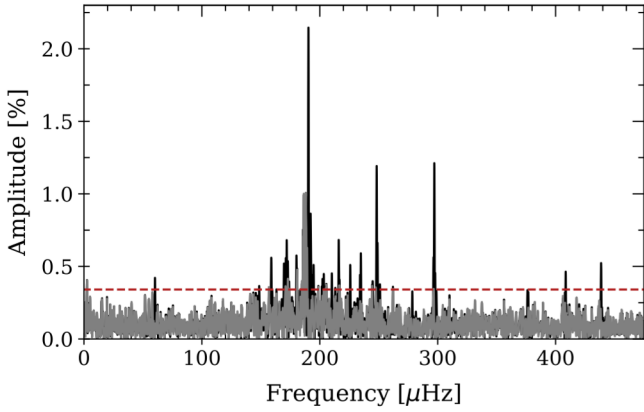

Figure 3. Periodogram of the GD 278 TESS data in black. In gray is the periodogram of the same data after prewhitening by the frequencies in Table 1. The red dashed line represents the 0.1% false alarm probability threshold, which we estimate to be 0.34%. Peaks above this line have a <0.1% chance of being caused by random noise and thus represent intrinsic signals from the star.

TESS. We show the 8.16 hr of overlapping data in Figure 4. Time is given in TESS Barycentric Julian Date (TBJD), which is the Julian Date at the solar system barycenter, offset by 2,457,000.0. The higher sampling rate (15 s) and signal-to-noise of the ground-based observations reveal shorter-timescale variations that are missed by the 2 minute cadence TESS data, especially the double-peaked feature located at roughly 1739.86 TBJD in Figure 4.

For better comparison, we have resampled the McDonald observations at the same 2 minute cadence of TESS. These data are plotted over each other in bottom panel of Figure 4 to highlight that the shortest-period features would be better resolved with future TESS observations obtained in the 20 second cadence mode. It is possible that our frequency solution in Table 1 lacks
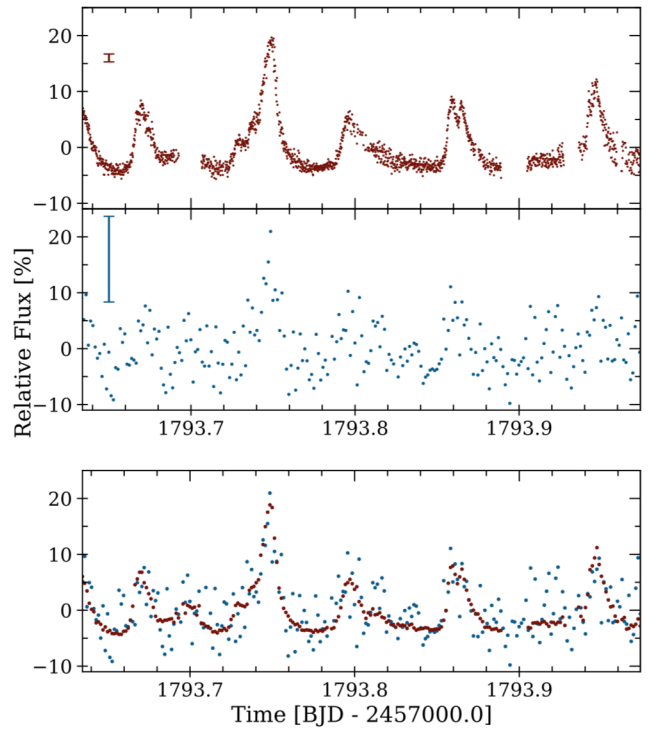

Figure 4. Top: simultaneous McDonald (15 s exposures) and TESS (120 s exposures) observations of GD 278, captured on 2019 November 8. A representative error bar is shown in the top left corner of each plot. Bottom: both data sets overplotted. The McDonald data (red) have been resampled to the same 2 minute cadence as the TESS data (blue).

some of the higher-frequency components that contribute to the peaky, nonlinear light-curve shape resolved by the McDonald observations. However, such modes are not independent pulsations

Table 2
Common Frequency Spacings That May Reveal the Identity (Especially the ℓ Values) of Eight Different Modes in GD 278

ID	ℓ	m	Period (s)	Frequency (μHz)	Amp. (%)	Splitting (μHz)
f_{1a}	1	-1	5135.1 ± 0.8	194.74 ± 0.03	0.47	
f_{1b}	1	0	$\mathbf{4756.5} \pm 0.7$	210.24 ± 0.03	0.47	15.50 ± 0.06
f_{1c}	1	1	4428.5 ± 0.5	225.812 ± 0.028	0.53	15.57 ± 0.06
f_{2a}	1	-1	4259.1 ± 0.5	234.79 ± 0.03	0.50	
f_{2b}	1	0	$\mathbf{4028.83} \pm 0.21$	248.211 ± 0.013	1.19	13.42 ± 0.04
f_{2c}^{*}	1	1	3815.8 ± 0.7	262.07 ± 0.05	0.32	13.85 ± 0.06
f_{3a}	1	-1	3365.56 ± 0.14	297.127 ± 0.012	1.25	
f_{3b}^{*}	1	$0^{\dagger}$	$\mathbf{3226.1} \pm 0.6$	309.98 ± 0.06	0.24	12.85 ± 0.07
f_{4a}	1	$0^{\dagger}$	$\mathbf{2658.51} \pm 0.28$	376.15 ± 0.04	0.35	
f_{4b}^{*}	1	$+1$	2569.0 ± 0.4	389.26 ± 0.06	0.26	13.10 ± 0.10
f_{5a}	1	-1	2447.86 ± 0.18	408.52 ± 0.03	0.46	
f_{5b}	1	0	$\mathbf{2367.4} \pm 0.21$			
f_{5c}^{*}	1	1	2292.0 ± 0.3	436.29 ± 0.06	0.26	$2 \times (13.89 \pm 0.09)$
f_{6a}	2	-2	6729.0 ± 1.8	148.61 ± 0.04	0.38	
f_{6b}	2	-1	5896.8 ± 1.1	169.58 ± 0.03	0.48	20.97 ± 0.07
f_{6c}	2	0	$\mathbf{5253.2} \pm 0.19$	190.359 ± 0.007	2.15	20.78 ± 0.04
f_{6d}^{*}	2	2	4270.8 ± 0.8	234.15 ± 0.05	0.32	$2 \times (21.89 \pm 0.05)$
f_{7a}	2	-2	6295.4 ± 1.0	158.846 ± 0.026	0.58	
f_{7b}	2	-1	5550.6 ± 0.8	180.161 ± 0.025	0.61	21.32 ± 0.05
f_{7c}	2	0	$\mathbf{4959.6} \pm 1.0$	201.63 ± 0.04	0.37	21.46 ± 0.07
f_{7d}^{*}	2	1	4473.1 ± 0.9	223.56 ± 0.05	0.32	21.93 ± 0.09
f_{7e}	2	2	4083.5 ± 0.7	244.89 ± 0.04	0.37	21.33 ± 0.09
f_{8a}	2	-1	5814.8 ± 0.7	171.975 ± 0.021	0.71	
f_{8b}	2	$0^{\dagger}$	$\mathbf{5198.3} \pm 0.8$	192.370 ± 0.029	0.53	20.39 ± 0.05
f_{8c}	2	$+1$	4628.8 ± 0.5	216.039 ± 0.022	0.68	23.67 ± 0.05

Note. Each multiplet is illustrated in Figures 5 and 6. In each subset we have attempted to identify the $m = 0$ central component critical for asteroseismic analysis; we use a dagger symbol (†) to identify uncertain $m = 0$ identifications. If a frequency present appears near where we might expect a rotationally split multiplet component but does not exceed the 0.34% significance threshold, we include it here but mark it with an asterisk (*).

and should not significantly affect our asteroseismic analysis in Section 4.

3.3. Orbital Period Measurement

In addition to pulsations, we also recover the spectroscopically determined orbital period of 4.6092 ± 0.0048 hr from Brown et al. (2020) in the TESS photometry. We detect a significant signal at 60.21 ± 0.03 μHz, which provides an independent measurement of the orbital period from the TESS data of 4.6142 ± 0.0022 hr, in good agreement with the period determined from spectroscopy and caused by the 209.1 ± 5.1 km s^{-1} radial-velocity variability of the ELM white dwarf. This photometric signal, with an amplitude in the TESS bandpass of $0.46 \pm 0.06\%$, may be caused by Doppler beaming of the white dwarf (Shporer et al. 2010; Hermes et al. 2014a).

3.4. Possible Multiplet Mode Identification

We find evidence for patterns in the observed periodogram that suggest common frequency spacings that could arise from rotational splittings if the ELM white dwarf is rotating at roughly 10 hr, which would cause $\ell = 1$ mode splittings of ≈ 13.7 μHz and $\ell = 2$ mode splittings of ≈ 21.5 μHz (e.g., Aerts 2021).

In total, we identify eight mode splittings in the GD 278 TESS periodogram: five that are consistent with $\ell = 1$ modes

and three $\ell = 2$ modes. In Table 2, we list 24 individual observed pulsation periods that make up eight groups, one for each multiplet. Also listed in Table 2 are the assumed ℓ and m numbers, periods, frequencies, amplitudes, and the splitting amount between adjacent modes within a group. We observe weighted mean rotational splittings of roughly 14.0 μHz for the $\ell = 1$ modes and 21.5 μHz for the $\ell = 2$ modes, both consistent with an overall rotation rate of roughly 10 hr.

The six modes with an asterisk have amplitudes less than the significance threshold; although these amplitudes lie below the significance threshold, we relax this threshold based on their location near predictions from common frequency splittings (e.g., Winget et al. 1991; Dunlap et al. 2010).

We show an illustration of the five $\ell = 1$ splittings in Figure 5. The location of the modes is indicated by the red tick marks, while the red dashed line represents the 0.1% false alarm probability threshold at 0.34% amplitude. In gray, we plot the periodogram of the original TESS data set. Over this periodogram, we plot in black a periodogram of the TESS data, after prewhitening by all periods listed in Table 2, not including the group of split modes being shown in a given subplot. In some cases (f_3 and f_4) we only identify two components, so it is not possible to unambiguously determine which of the two components corresponds to the central ($m = 0$) mode. There is therefore ambiguity on which modes should be considered the $m = 0$ mode used for the asteroseismic analysis in Section 4.
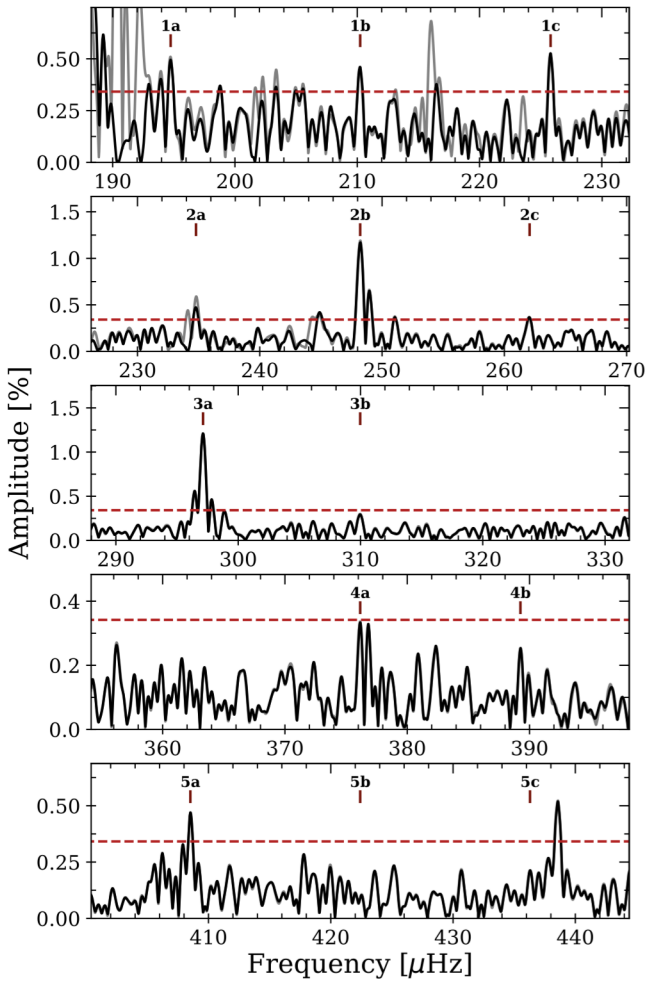
Figure 5. Possible evidence for five $\ell = 1$ mode splittings, identified within the GD 278 TESS periodogram and listed in Table 2. Red tick marks indicate the frequencies that we propose form rotationally split multiplets, consistent with an overall 10 hr rotation rate. For each mode we show in gray the prewhitened TESS light curve, subtracted of all frequencies listed in Table 1 other than those indicated by the red points, and show the resulting periodogram in black. The red dashed lines mark the 0.34% significance threshold.

We repeat this illustration for the three identified $\ell = 2$ modes in Figure 6, this time indicating the location of the modes by blue tick marks. One of the $\ell = 2$ modes (f_8) only has three identified components, which again leads to ambiguity in determining which of the three components corresponds to the $m = 0$ mode.

4. Asteroseismic Modeling

The $m = 0$ modes we identify in Table 2 serve as the baseline for our asteroseismic investigation into GD 278, offering us five likely $\ell = 1$ modes and three likely $\ell = 2$ modes observed in this pulsating white dwarf. For completeness, our full asteroseismic analysis explores solutions using all 12 different possible combinations of identified $m = 0$ modes from the ambiguous $\ell = 1$ modes of f_3 and f_4 as well as the ambiguous $\ell = 2$ mode of f_8.

4.1. Initial Expectations from MESA Modeling

As an initial pass at guiding expectations, we generated a model of the ELM white dwarf GD 278 using the stellar evolution code MESA version r12115 (Paxton et al. 2011,
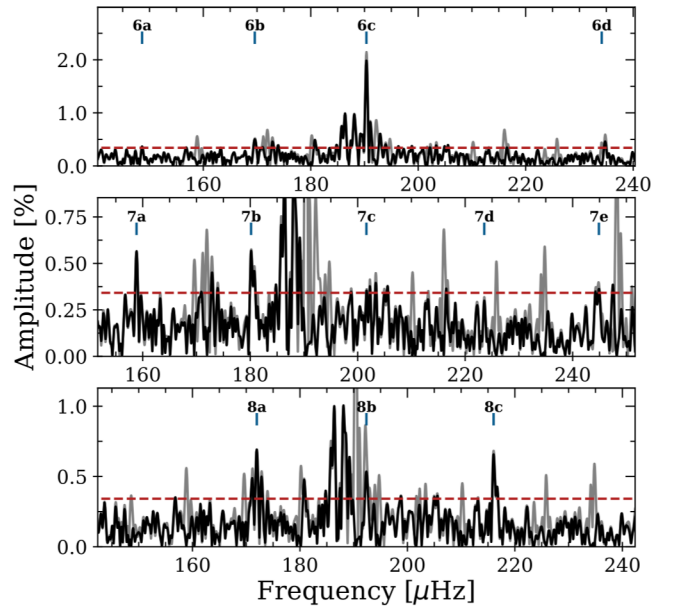
Figure 6. Similar to Figure 5, except for the three $\ell = 2$ mode splittings identified identified within the GD 278 TESS periodogram and listed in Table 2. Blue tick marks indicate the frequencies that we propose form the rotationally split multiplets, also consistent with 10 hr rotation.

2013, 2015, 2018, 2019). Our input model to generate a $0.19\,M_\odot$ ELM white dwarf followed the inlists first described by Istrate et al. (2016b), which evolve a close binary and include element diffusion and rotational mixing. In short, we start with a $1.1\,M_\odot$, $Z = 0.0142$ metallicity ZAMS progenitor in a 2.90 day binary with a $1.4\,M_\odot$ companion and evolve the system through mass loss until the remnant is a $0.19\,M_\odot$ ELM white dwarf; further details are discussed in Istrate et al. (2016b).

We evolved this ELM white dwarf model through its many diffusion-induced CNO flashes (e.g., Althaus et al. 2001; Panei et al. 2007; Althaus et al. 2013) until it arrived at the final cooling track then we paused the evolution at 9180 K. Here our $0.1904\,M_\odot$ model has a surface gravity of $\log g = 6.644$, a hydrogen-layer mass of $M_H = 8.2 \times 10^{-4} M_\star$, a radius of $R_\star = 0.03443 R_\odot$, and a luminosity of $L_\star = 7.56 \times 10^{-3} L_\odot$. We artificially smoothed the Brunt–Väisälä frequency from this static model with a built-in weighted smoothing in MESA using eight cells (rather than the default two cells), in order to avoid any numerical noise dominating our resultant pulsation frequencies.

We took the output of this smoothed MESA model and pulsated it using GYRE (Townsend & Teitler 2013) to generate an output set of expected non-radial pulsation modes. We did not attempt to generate a grid of models to explore to perform a full asteroseismic fit but first sought to understand the possible radial order of the observed modes in GD 278 from the TESS observations. We compare the observed periods to the theoretical MESA predictions in Table 3 and especially note that these are not fits but rather the output of a model selected to match the spectroscopy of GD 278. As a reminder, the atmospheric parameters from spectroscopy by Brown et al. (2020) include the 3D corrections of Tremblay et al. (2015) and find $T_{\rm eff} = 9230 \pm 100$ K and $\log g = 6.627 \pm 0.056$, which corresponds to a mass of $0.191 \pm 0.013\,M_\odot$.

ID	Π^O (s)	Π^T (s)	ℓ	k	$\delta\Pi$ (s)
f_1	4756.5	4761.8	1	56	−5.3
f_2	4028.83	4020.8	1	47	8.0
f_3	3226.1	3204.6	1	37	21.5
f_4	2658.51	2637.7	1	30	20.8
f_5	2367.4	2395.0	1	27	−27.6
f_6	5253.2	5270.2	2	108	−17.0
f_7	4959.6	4932.8	2	101	26.8
f_8	5198.3	5221.8	2	107	−23.5

Note. The observed periods identified in Table 2 are also included (Π^O). This
model has $1/\chi^2 = 0.0024$ (see Equation (1)).

This Mesa model features an overall $\ell = 1$ asymptotic mean
period spacing of roughly 83 s, and an $\ell = 2$ mean period
spacing of roughly 48 s. The observed period range in Table 3
implies that the $\ell = 1$ modes have radial orders ranging from
$27 < k < 56$, with $\ell = 2$ modes of especially high radial order,
ranging from $101 < k < 108$.

Our stellar model includes rotation, with the initial rotation
velocity set such that the star is synchronized with the initial
orbital period. Moreover, we take into account the effect of tides
and spin–orbit coupling. Given this, we note that this final MESA
model has an 11.6 hr surface rotation period. Interestingly, the
model is rotating marginally differentially, a consequence
imprinted in the CNO flashing episodes (see Section 4.1.1 in
Istrate et al. 2016b). If the rotational splittings we identify in
Section 3.4 are correct, this model predicts rotation at almost
exactly the same rate as observed in GD 278.

We can also estimate the expected distance to this white
dwarf by comparing the luminosity of the model ($L_\star = 0.00756$
$L_\odot$) to the Gaia apparent magnitude ($G = 14.88$ mag). Using
the 3D reddening map of Green et al. (2019), we find that the
effects of reddening do not become an issue at the coordinates
of GD 278 until >200 pc, so we assume no reddening
coefficient. We use the bolometric correction of Choi et al.
(2016) for an object with $T_{\rm eff} = 9250$ K and $\log g = 6.5$. We
obtain a seismic distance of 104.4 pc. This is significantly
discrepant with the parallax distance determined from Gaia
eDR3 of 151.19 ± 0.78 pc (Bailer-Jones et al. 2021), suggest-
ing our model is underluminous compared to that needed to
explain the measured Gaia parallax.

4.2. Asteroseismic Fits with LPCODE

We further analyzed the identified periods observed in
GD 278 using the low-mass white dwarf models of Calcaferro
et al. (2018). In short, the models expand upon the ELM white
dwarf models described in Althaus et al. (2013) generated
using the LPCODE stellar evolution code. This code computes
in detail the complete evolutionary stages that lead to white
dwarf formation, allowing the study of white dwarf evolution
consistently with the predictions of the evolutionary history of
the progenitors (see Althaus et al. 2005, 2013, 2015 for details).
For ELM white dwarfs, LPCODE computes initial models by
mimicking the binary evolution of progenitor stars (Althaus
et al. 2013). Adiabatic pulsation periods for non-radial dipole

($\ell = 1$) and quadrupole ($\ell = 2$) g modes were computed
employing the adiabatic version of the LP-PUL pulsation
code (see Córsico & Althaus 2006 for details). The models of
low-mass white dwarfs we employ in this work include not just
canonically thick hydrogen layers but also include new
evolutionary sequences of thinner envelopes (Calcaferro et al.
2018).

We searched a grid of ELM white dwarf models for the best-fit
solution in a broad range of effective temperatures (8500–9800 K),
overall mass (0.15–0.44 $M_\odot$), and hydrogen envelope thicknesses
in the interval $-5.8 \lesssim \log(M_H/M_\star) \lesssim -1.7$ (depending on the
stellar mass). Eventually we restricted our attention to the region
within roughly 4σ of the overall mass determined from the
spectroscopic parameters (0.15–0.24 $M_\odot$).

Using this grid of models, we searched the 12 different
period solutions that arise from the ambiguity of the f_3, f_4, and
f_8 splittings (Section 3.4), fitting only the $m = 0$ modes. We
explored best-fit models for each of the 12 period solutions,
both restricted to the narrow range around the spectroscopic
solution and across the broader range of overall stellar mass
and effective temperature. Our best-fit models were optimized
to minimize a quality function (χ^2) that considers the
differences between the observed pulsation periods, Π^O, and
theoretical pulsation periods, Π^T, and is defined as

$$\chi^2(M_\star, T_{\rm eff}, M_H) = \frac{1}{N}\sum_{i=1}^{N}(\Pi_i^O - \Pi_i^T)^2 \qquad (1)$$

where $M_\star$ is the stellar mass, $T_{\rm eff}$ is the effective temperature,
M_H is the mass fraction of the hydrogen envelope, and N is the
number of observed pulsation periods. For this procedure, we
fix the values of ℓ at the outset according to the identifications
in Table 2.

Unfortunately, there is not a global minimum preferred fit
within the 1σ bounds provided by the spectroscopy of Brown
et al. (2020). For all 12 period solutions, the ELM white dwarf
model with the formal best fit to the observed $m = 0$ pulsation
periods occurs with a stellar mass of 0.239 $M_\odot$, an effective
temperature between $9680-9710$ K, and a hydrogen-layer
mass of roughly $M_H = 3.6 \times 10^{-3} M_\star$.

As all 12 period solutions return similar (though not
identical) quality maps, we restrict further discussion to only
the solution defined explicitly in Table 2. The quality of the fit
to the observed periods for this solution across all effective
temperatures and stellar masses is shown in Figure 7. Each
point ($M_\star$, $T_{\rm eff}$) in the map corresponds to a hydrogen-layer
mass ($M_H/M_\star$) that maximizes the value of $1/\chi^2$ for that stellar
mass and effective temperature. The green box represents the
1σ bounds of the mass and effective temperature obtained from
spectroscopy. For this model, the formal best (global) solution
has $1/\chi^2 = 0.0154$, with an overall mass of 0.239 $M_\odot$, a
hydrogen-layer mass of $M_H = 3.55 \times 10^{-3} M_\star$ and an effective
temperature of 9698 K. Notably, this model is $>3\sigma$ in tension
with both the observed spectroscopic effective temperature
and mass.

Similar to Section 4.1, we estimate the distance to this white
dwarf by comparing the seismic luminosity of the global best-
fit model ($L_\star = 0.00645\ L_\odot$) to the Gaia apparent magnitude.
We obtain a seismic distance of 96.4 pc for this model. Again,
this value is significantly discrepant with the 151.19 ± 0.78 pc
parallax distance (Bailer-Jones et al. 2021).

If we restrict our fits and require them to be within a 1σ box
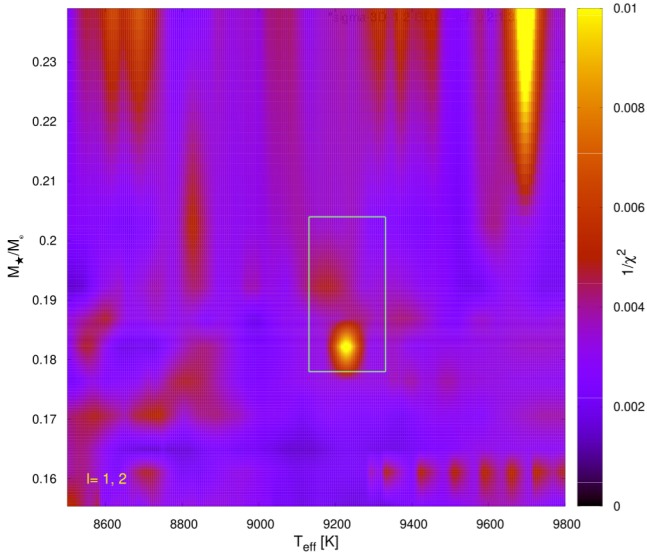consistent with the spectroscopic parameters, the best-fit model

Figure 7. Map of the inverse of the quality function $(1/\chi^2)$ as a function of the stellar mass $(M_\star)$ and effective temperature $(T_{\rm eff})$, considering the eight $m = 0$ modes identified in bold in Table 2. Each point on the map corresponds to a hydrogen envelope mass (M_H) that maximizes the value of $1/\chi^2$. The green box represents the GD 278 spectroscopic mass, effective temperature, and the corresponding 1σ uncertainties from Brown et al. (2020).

Table 4
Properties of the Best-fit Asteroseismic Model for GD 278 Using the LPCODE
Evolution Code, Restricted to within 1σ of the Spectroscopic Parameters,
Where All Modes are Assumed to be the $m = 0$ Components Identified in
Table 2

ID	Π^O (s)	Π^T (s)	ℓ	k	$\delta\Pi$ (s)
f_1	4756.5	4760.13	1	46	−3.63
f_2	4028.83	4043.10	1	38	−14.27
f_3	3226.1	3238.14	1	31	−12.04
f_4	2658.51	2644.92	1	25	13.59
f_5	2367.4	2355.23	1	22	12.17
f_6	5253.2	5253.85	2	88	−0.65
f_7	4959.6	4956.15	2	83	3.45
f_8	5198.3	5194.41	2	87	3.89

Note. The characteristics of this best-fit model are as follows: $M_\star = 0.182\,M_\odot$, $M_H = 3.1 \times 10^{-6}M_\star$, $T_{\rm eff}$=9226 K, $L_\star = 6.12 \times 10^{-3}L_\odot$, $\log g = 6.727$, $R_\star = 0.0306R_\odot$, and $1/\chi^2 = 0.0111$.

frequency separations consistent to within 2σ, and the implied rotation rate agrees for both the $\ell = 1$ and $\ell = 2$ modes independently.

It is also possible that even if we have correctly identified all eight $m = 0$ modes present, the relatively long periods in GD 278 have such high radial order that none of the modes are particularly sensitive to interior structure transitions. These long-period modes may not lend themselves to a strongly favored, unique global solution, as seen in some higher-mass DAVs (e.g., Giammichele et al. 2017).

4.3. Search for a Mean Period Spacing

Based on some of the ambiguities in the asteroseismic analysis, we sought to constrain at least the mean density of the ELM white dwarf GD 278 by trying to measure and then analyze the observed mean period spacing, which approximates the overall mean density and thus overall mass of the star using the g-mode pulsations present (Althaus et al. 2010).

First, we attempted to search for a roughly constant period spacing in our observations. Since we cannot know the radial order (k) of the modes a priori, we first searched for any sign in the data for recurring period spacings. The long-period pulsations present (>2300 s) imply relatively high radial orders ($k > 20$), so the period spacing between modes should be asymptotic and nearly constant (Tassoul 1980).

We initially searched for patterns in the period spacing in the data itself by taking a period transform of the period transform; in short, we inverted the Lomb–Scargle periodogram in Figure 3 so that it was in period and not frequency, and then took the period transform of this period transform (e.g., Winget et al. 1991) within the range of all pulsation power (2000–8000 s). This is shown in Figure 8. Unfortunately, this did not reveal any dominant peaks, so was not valuable for determining recurrent period spacings in the data themselves.

As a next step, we searched for a constant period spacing using three additional tests (e.g., Calcaferro & Córsico 2017b). In short, we ignored our mode identifications and searched all significant frequencies given in Table 1 using a Kolmogorov–Smirnov test (K–S test; Kawaler 1988), an inverse variance test (I–V test; O'Donoghue 1994), and the Fourier transform test (F–T test; Handler et al. 1997). The results of the three tests are shown in Figure 9. There are some suggestive indications of
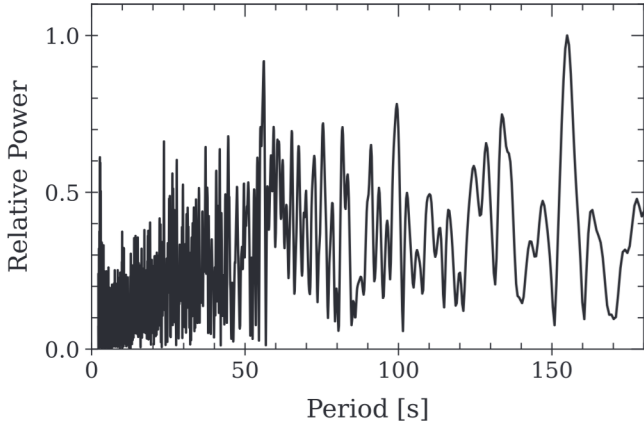
occurs at an overall mass of $0.1822\,M_\odot$ (with $\log g = 6.727$) and an effective temperature of 9226 K, with an extremely thin hydrogen-layer mass of $M_H = 3.08 \times 10^{-6}M_\star$, more than three orders of magnitude thinner than the global best-fit model, as well as the exploratory MESA model in Section 4.1. This restricted solution has a goodness-of-fit value of $1/\chi^2 = 0.0111$. Our period solution and radial orders of this restricted best fit are described in Table 4. The observed period range in Table 4 implies that the $\ell = 1$ modes have radial orders of $22 < k < 46$, with $\ell = 2$ modes ranging from $83 < k < 88$. For this model, with $L_\star = 0.00612\,L_\odot$, we find a seismic distance of 93.9 pc.

This thin-hydrogen-layer solution at $0.182\,M_\odot$ is the most commonly occurring restricted best fit (in 8 of 12 cases), and in all 8 cases implies an $\ell = 1$ mean period spacing of roughly 100.0 s. In the other 4 cases, the best restricted fit (within 1σ of the spectroscopic parameters) occurs with models featuring an overall mass of $0.192\,M_\odot$, effective temperatures ranging from $9340-9360$ K, and a thicker hydrogen-layer mass of $M_H = 2.38 \times 10^{-4}M_\star$. With the slightly higher overall mass, the $\ell = 1$ mean period spacing for these models is roughly 91.4 s. The goodness-of-fit parameter for the $0.192\,M_\odot$ solution is worse than the $0.182\,M_\odot$ solution, with $1/\chi^2 = 0.0093$. However, it is most proximate to the spectroscopic values without invoking an artificially stripped hydrogen-layer mass that is much thinner than what is expected from stellar evolution (Panei et al. 2007; Steinfadt et al. 2010).

Given that our absolute best-fit model across all parameters disagrees significantly with the spectroscopic parameters, we are reluctant to use our asteroseismic analysis to adopt an overall stellar model. This could implicate our mode identifications and our assumption of a roughly 10 hr rotation period in Section 3.4 as being systematically incorrect. We note that some of our splittings within the same multiplet are inconsistent; for example, the three modes in f_2 have frequency spacings that are formally $>4\sigma$ discrepant. However, the vast majority of rotational multiplets identified in Table 2 have

Figure 8. Period transform of the GD 278 Lomb–Scargle periodogram shown in Figure 3. Unfortunately, we cannot see any clear recurrent period spacings in the periodogram itself.
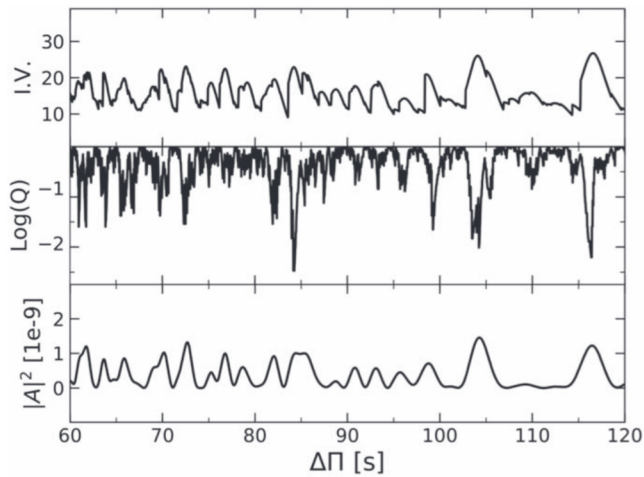

Figure 9. We searched for a constant period spacing among all detected significant pulsation frequencies listed in Table 1 using three tests: an inverse variance test (top panel), a Kolmogorov–Smirnov test (middle panel), and a Fourier transform test (bottom panel). The strongest signals emerge at roughly 104 s, 84 s, 116 s, and 72.5 s, and are put into context in Figure 10.

constant period spacings at roughly 72.5 s, 84 s, 104 s, and 116 s, most prominently at 84 s.

To put these mean period spacings into context, we show in Figure 10 a series of expected period spacings as a function of effective temperature for a suite of ELM white dwarf models with masses between 0.15 and 0.44 $M_{\odot}$ (described in Section 4.2). All models have the thickest possible (canonical) hydrogen-layer masses: sequences with $M_{\star} < 0.18\,M_{\odot}$ are characterized by $M_H \approx 10^{-2} M_{\star}$ (since these model ELM white dwarfs do not undergo CNO flashes), while those with $M_{\star} > 0.18\,M_{\odot}$ have $M_H < 2 \times 10^{-3} M_{\star}$. The effective temperature constraints from spectroscopy are shown as vertical cyan lines.

Figure 10 shows that the 116 s possible period spacing is not within the range expected for $\ell = 1$ modes of ELM white dwarfs. The roughly 104 s, 84 s, and 72.5 s period spacings would imply values of the overall stellar masses lower than 0.14 $M_{\odot}$, roughly 0.20 $M_{\odot}$, and roughly 0.24 $M_{\odot}$, respectively. The two $\ell = 1$ mean period spacings in Figure 9 at 104 s and 84 s are marked with horizontal orange lines. We also repeated
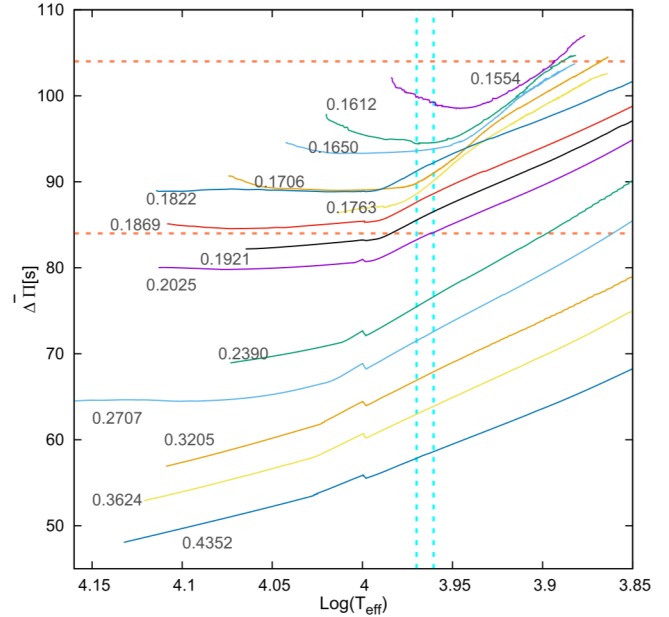
Figure 10. Average of the computed dipole period spacings for $\ell = 1$ modes as a function of effective temperature for various cooling models of ELM white dwarfs (Calcaferro et al. 2018) with masses between 0.15–0.44 $M_{\odot}$ and canonically thick hydrogen envelopes. Plotted over these models are the two possible values of the constant period spacing for GD 278 found from our analysis in Figure 9 (roughly 84 s and 104 s, horizontal lines), as well as bounds from the spectroscopic effective temperature and uncertainties (vertical cyan lines). For white dwarfs $<0.2\,M_{\odot}$ we expect mean period spacings $\overline{\Delta\Pi} > 80$ s.

the exercise shown in Figure 9 on the smaller list of eight likely $m = 0$ modes from Table 2, which includes a mix of $\ell = 1$ and $\ell = 2$ modes. We do not visualize this result but these tests show slight preference for possible mean period spacings at roughly 62 s and 72 s, which fall at an unexpected range based on previous spectroscopy of GD 278, so we do not discuss those tests further.

The strongest response to the K–S test in Figure 9 occurs at roughly 84 s, which is very similar to the $\ell = 1$ mean period spacing of roughly 82 s that we expect from our MESA modeling described in Section 4.1 for a white dwarf of the given spectroscopic parameters and a canonically thick hydrogen layer. However, the ambiguity of this signal and the mode identification presented in Table 2 precludes closing the chapter on asteroseismic investigation of GD 278 until we can find a significantly best-fit solution. Improved fits are likely to come from utilizing the precise parallax distance from Gaia, which we leave to future work.

5. Discussion and Conclusions

We discovered GD 278 as part of a search of the Gentile Fusillo et al. (2019) Gaia DR2 catalog of white dwarfs for pulsating ELM white dwarfs. It was selected for its position on the Gaia color–magnitude diagram relative to other known pulsators and on its intrinsic variability, which we inferred from its Gaia G-band flux uncertainty. This method for selecting candidate variable stars was described further by Guidry et al. (2021), who used the method to confirm 32 new DAVs and one new pulsating ELM white dwarf.

GD 278 stood out as a likely variable candidate and we confirmed its pulsations from the McDonald Observatory in

2019 before it was announced as a bona fide ELM white dwarf in a 4.61 hr single-lined binary by Brown et al. (2020), selected from an existing catalog of bright white dwarfs (Raddi et al. 2017). Our ground-based discovery of pulsations allowed us to obtain 2 minute cadence observations with TESS, obtaining the first space-based photometry of a pulsating ELM white dwarf. This revealed the richest set of oscillation periods ever obtained for an ELM white dwarf.

However, mode identification of the frequencies in Table 2 was a particular challenge, with rotational splitting exceeding the frequency differences between adjacent radial overtones. One method for identifying the spherical degree (ℓ) is to look for triplets or quintuplets of modes with frequencies consecutively split by equal amounts. For GD 278, we identified five possible $\ell = 1$ splittings and three possible $\ell = 2$ splittings, many overlapping with one another. The $\ell = 1$ modes we observe have a mean frequency separation of $\approx 14.0 \, \mu$Hz and the $\ell = 2$ modes are separated from one another by $\approx 21.5 \, \mu$Hz; both are consistent with an overall rotation period of roughly 10 hr. This is the first direct estimate of the rotation rate of an ELM white dwarf. The role of rotation is likely vital for understanding the frequent occurrence of heavy metals in the atmospheres of ELM white dwarfs (Hermes et al. 2014b; Istrate et al. 2016b, 2016a).

We recover the 4.6092 ± 0.0048 hr orbital period from the spectroscopy of Brown et al. (2020) in the TESS photometry, finding a marginal but significant variation at 4.6142 ± 0.0022 hr. The 4.61 hr orbital period of GD 278 is very close to the 4.5912 ± 0.0012 hr orbital period of SDSS J184037.78+642312.3, which was the first ELM white dwarf discovered to exhibit pulsations (Hermes et al. 2012). That work notes that a pulsating ELM white dwarf with a rotation period of 4.6 hr would have $\ell = 1$ modes split into components separated by 30 μHz, but a 4.6 hr orbital period is likely not short enough for the white dwarf to have synchronized with the orbital period through tidal dissipation (Fuller & Lai 2013). Models by Istrate et al. (2016b) show that low-mass white dwarfs can have rotation rates several times faster than their orbital period upon arrival on the cooling track.

We detected a significant pulsation mode in GD 278 at 6729.0 ± 1.8 s, which is so far the longest pulsation period detected in a white dwarf. Previously, SDSS J222859.93+362359.6 had the longest detected pulsation period at 6234.9 ± 6.0 s. That object also happens to be the coolest known pulsating ELM white dwarf with $T_{\rm eff} = 7870 \pm 120$ K (Hermes et al. 2013b). However, extensive monitoring of SDSS J222859.93+362359.6 does not show radial-velocity variability. Unless this object is in an orbit with a low inclination, it may not actually be an ELM white dwarf (Bell et al. 2017).

We see marginal evidence from a K–S test of all pulsation modes present that there is a roughly 84 s mean period spacing, which is what we expect from asteroseismic models of a roughly $0.20 \, M_\odot$ ELM white dwarf computed by both MESA and the LPCODE stellar evolution codes, assuming the star has a thick hydrogen layer. While we do not adopt a formally best-fit asteroseismic fit with our exploration of a grid of models using LPCODE, we do find that there are asteroseismic solutions for our TESS observations of GD 278 with parameters that are consistent with those found from spectroscopy (Brown et al. 2020), however, further inferred luminosities/distances do not agree. Given the large number of variables that lead to these conclusions, it is difficult to explain the discrepancies.

With continued monitoring of GD 278, it may be possible to measure rates of change of the significant frequencies within the star, which in general are related to the cooling rate of the white dwarf and the rate of change of the white dwarf radius (Winget & Kepler 2008). There are no significant constraints yet on rates of period change for ELM white dwarfs, but these rates of period change would be incredibly valuable at distinguishing whether the ELM white dwarf has undergone CNO flashes in its past (Calcaferro et al. 2017a). Unfortunately, GD 278 will not be observed by TESS in Cycle 4, but hopefully it will again in a future extended mission. Starting with Cycle 5, full-frame images will be saved every 200 s, enabling asteroseismic study of even more bright ELM white dwarfs.

ORCID iDs

Isaac D. Lopez ⓘ https://orcid.org/0000-0002-0009-409X
J. J. Hermes ⓘ https://orcid.org/0000-0001-5941-2286
Leila M. Calcaferro ⓘ https://orcid.org/0000-0002-1345-8075
Keaton J. Bell ⓘ https://orcid.org/0000-0002-0656-032X
Adam Samuels ⓘ https://orcid.org/0000-0003-1895-2934
Zachary P. Vanderbosch ⓘ https://orcid.org/0000-0002-0853-3464
Alejandro H. Córsico ⓘ https://orcid.org/0000-0002-0006-9900
Alina G. Istrate ⓘ https://orcid.org/0000-0002-8811-8171

References

Aerts, C. 2021, RvMP, 93, 015001
Althaus, L. G., Camisassa, M. E., Miller Bertolami, M. M., Córsico, A. H., & García-Berro, E. 2015, A&A, 576, A9

Althaus, L. G., Córsico, A. H., Isern, J., & García-Berro, E. 2010, A&ARv, 18, 471
Althaus, L. G., Miller Bertolami, M. M., & Córsico, A. H. 2013, A&A, 557, A19
Althaus, L. G., Serenelli, A. M., & Benvenuto, O. G. 2001, MNRAS, 323, 471
Althaus, L. G., Serenelli, A. M., Panei, J. A., et al. 2005, A&A, 435, 631
Amaro-Seoane, P., Audley, H., Babak, S., et al. 2017, arXiv:1702.00786
Bailer-Jones, C. A. L., Rybizki, J., Fouesneau, M., Demleitner, M., & Andrae, R. 2021, AJ, 161, 147
Bell, K. J. 2020, AAS Meeting Abstracts, 235, 106.06
Bell, K. J., Gianninas, A., Hermes, J. J., et al. 2017, ApJ, 835, 180
Bell, K. J., Kepler, S. O., Montgomery, M. H., et al. 2015, in ASP Conf. Ser., 493, 19th European Workshop on White Dwarfs, ed. P. Dufour, P. Bergeron, & G. Fontaine (San Francisco, CA: ASP), 217
Bell, K. J., Pelisoli, I., Kepler, S. O., et al. 2018, A&A, 617, A6
Brown, W. R., Gianninas, A., Kilic, M., Kenyon, S. J., & Allende Prieto, C. 2016, ApJ, 818, 155
Brown, W. R., Kilic, M., Allende Prieto, C., Gianninas, A., & Kenyon, S. J. 2013, ApJ, 769, 66
Brown, W. R., Kilic, M., Allende Prieto, C., & Kenyon, S. J. 2010, ApJ, 723, 1072
Brown, W. R., Kilic, M., Allende Prieto, C., & Kenyon, S. J. 2012, ApJ, 744, 142
Brown, W. R., Kilic, M., Kosakowski, A., et al. 2020, ApJ, 889, 49
Calcaferro, L. M., Córsico, A. H., & Althaus, L. G. 2017a, A&A, 600, A73
Calcaferro, L. M., Córsico, A. H., & Althaus, L. G. 2017b, A&A, 607, A33
Calcaferro, L. M., Córsico, A. H., Althaus, L. G., Romero, A. D., & Kepler, S. O. 2018, A&A, 620, A196
Choi, J., Dotter, A., Conroy, C., et al. 2016, ApJ, 823, 102
Córsico, A. H., & Althaus, L. G. 2006, A&A, 454, 863
Córsico, A. H., Althaus, L. G., Miller Bertolami, M. M., & Kepler, S. O. 2019, A&ARv, 27, 7
Driebe, T., Schoenberner, D., Bloecker, T., & Herwig, F. 1998, A&A, 339, 123
Dunlap, B. H., Barlow, B. N., & Clemens, J. C. 2010, ApJL, 720, L159
Fontaine, G., & Brassard, P. 2008, PASP, 120, 1043
Fuller, J., & Lai, D. 2013, MNRAS, 430, 274
Gaia Collaboration, Prusti, T., de Bruijne, J. H. J., et al. 2016, A&A, 595, A1
Gentile Fusillo, N. P., Tremblay, P.-E., Gänsicke, B. T., et al. 2019, MNRAS, 482, 4570
Giammichele, N., Charpinet, S., Brassard, P., & Fontaine, G. 2017, A&A, 598, A109
Gianninas, A., Kilic, M., Brown, W. R., Canton, P., & Kenyon, S. J. 2015, ApJ, 812, 167
Green, G. M., Schlafly, E., Zucker, C., Speagle, J. S., & Finkbeiner, D. 2019, ApJ, 887, 93
Guidry, J. A., Vanderbosch, Z. P., Hermes, J. J., et al. 2021, ApJ, 912, 125
Handler, G., Pikall, H., O'Donoghue, D., et al. 1997, MNRAS, 286, 303
Harris, C. R., Millman, K. J., van der Walt, S. J., et al. 2020, Natur, 585, 357
Hermes, J. J., Brown, W. R., Kilic, M., et al. 2014a, ApJ, 792, 39
Hermes, J. J., Gänsicke, B. T., Kawaler, S. D., et al. 2017, ApJS, 232, 23

Hermes, J. J., Gänsicke, B. T., Koester, D., et al. 2014b, MNRAS, 444, 1674
Hermes, J. J., Montgomery, M. H., Winget, D. E., et al. 2012, ApJL, 750, L28
Hermes, J. J., Montgomery, M. H., Winget, D. E., et al. 2013a, ApJ, 765, 102
Hermes, J. J., Montgomery, M. H., Gianninas, A., et al. 2013b, MNRAS, 436, 3573
Hunter, J. D. 2007, CSE, 9, 90
Iben, Icko J., & Livio, M. 1993, PASP, 105, 1373
Iben, Icko J., & Tutukov, A. V. 1986, ApJ, 311, 742
Istrate, A. G., Fontaine, G., Gianninas, A., et al. 2016a, A&A, 595, L12
Istrate, A. G., Marchant, P., Tauris, T. M., et al. 2016b, A&A, 595, A35
Kanodia, S., & Wright, J. 2018, RNAAS, 2, 4
Kawaler, S. D. 1988, in IAU Symp. 123, Advances in Helio- and Asteroseismology, ed. J. Christensen-Dalsgaard & S. Frandsen (Dordrecht: D. Reidel), 329
Kepler, S. O., Kleinman, S. J., Nitta, A., et al. 2007, MNRAS, 375, 1315
Kilic, M., Brown, W. R., Allende Prieto, C., et al. 2011, ApJ, 727, 3
Kilic, M., Brown, W. R., Allende Prieto, C., et al. 2012, ApJ, 751, 141
Kilic, M., Hermes, J. J., Córsico, A. H., et al. 2018, MNRAS, 479, 1267
Kilic, M., Hermes, J. J., Gianninas, A., & Brown, W. R. 2015, MNRAS, 446, L26
Kilic, M., Stanek, K. Z., & Pinsonneault, M. H. 2007, ApJ, 671, 761
Kosakowski, A., Kilic, M., Brown, W. R., & Gianninas, A. 2020, ApJ, 894, 53
Lightkurve Collaboration, Cardoso, J. V. d. M., Hedges, C., et al. 2018, Lightkurve: Kepler and TESS time series analysis in Python, Astrophysics Source Code Library, ascl:1812.013
Marsh, T. R., Dhillon, V. S., & Duck, S. R. 1995, MNRAS, 275, 828
Montgomery, M. H., Hermes, J. J., Winget, D. E., Dunlap, B. H., & Bell, K. J. 2020, ApJ, 890, 11
O'Donoghue, D. 1994, MNRAS, 270, 222
Paczynski, B. 1976, in IAU Symp. 73, Structure and Evolution of Close Binary Systems, ed. P. Eggleton, S. Mitton, & J. Whelan (Dordrecht: D. Reidel), 75
Panei, J. A., Althaus, L. G., Chen, X., & Han, Z. 2007, MNRAS, 382, 779
Paxton, B., Bildsten, L., Dotter, A., et al. 2011, ApJS, 192, 3
Paxton, B., Cantiello, M., Arras, P., et al. 2013, ApJS, 208, 4
Paxton, B., Marchant, P., Schwab, J., et al. 2015, ApJS, 220, 15
Paxton, B., Schwab, J., Bauer, E. B., et al. 2018, ApJS, 234, 34
Paxton, B., Smolec, R., Schwab, J., et al. 2019, ApJS, 243, 10
Pelisoli, I., Kepler, S. O., & Koester, D. 2018a, MNRAS, 475, 2480
Pelisoli, I., Kepler, S. O., Koester, D., et al. 2018b, MNRAS, 478, 867
Pelisoli, I., & Vos, J. 2019, MNRAS, 488, 2892
Raddi, R., Gentile Fusillo, N. P., Pala, A. F., et al. 2017, MNRAS, 472, 4173
Ricker, G. R., Winn, J. N., Vanderspek, R., et al. 2015, JATIS, 1, 014003
Shporer, A., Kaplan, D. L., Steinfadt, J. D. R., et al. 2010, ApJL, 725, L200
Steinfadt, J. D. R., Bildsten, L., & Arras, P. 2010, ApJ, 718, 441
Tassoul, M. 1980, ApJS, 43, 469
Tody, D. 1986, Proc. SPIE, 627, 733
Townsend, R. H. D., & Teitler, S. A. 2013, MNRAS, 435, 3406
Tremblay, P. E., Bergeron, P., & Gianninas, A. 2011, ApJ, 730, 128
Tremblay, P. E., Gianninas, A., Kilic, M., et al. 2015, ApJ, 809, 148
Winget, D. E., & Kepler, S. O. 2008, ARA&A, 46, 157
Winget, D. E., Nather, R. E., Clemens, J. C., et al. 1991, ApJ, 378, 326
Wu, Y. 2001, MNRAS, 323, 248